Chemical Science

ROYAL SOCIETY OF CHEMISTRY

EDGE ARTICLE

View Article Online
View Journal | View Issue

Check for updates

Cite this: *Chem. Sci.*, 2022, **13**, 9719

All publication charges for this article have been paid for by the Royal Society of Chemistry

# Single-molecule photosensitizers for NIR-II fluorescence and photoacoustic imaging guided precise anticancer phototherapy†‡

Hua Gu,[a] Weijian Liu,[a] Wen Sun,[ab] Jianjun Du,[ab] Jiangli Fan*[ab] and Xiaojun Peng[a]

Received 23rd May 2022
Accepted 15th July 2022

DOI: 10.1039/d2sc02879d

rsc.li/chemical-science

It is ideal yet challenging to achieve precise tumor targeting and high-quality imaging guided combined photodynamic and photothermal therapy (PDT and PTT). In this study, we synthesized a series of D–π–A-type single-molecule photosensitizers (**CyE-TT**, **CyQN-TT**, and **CyQN-BTT**) based on quaternized 1,1,2-trimethyl-1*H*-benz[*e*]indoles as acceptors by introducing π-bridges to elongate their emission wavelength and triphenylamine as a donor to construct a twisted molecular conformation. We found that the $^1O_2$ generation ability and the photothermal conversion efficiency (PCE) are directly correlated with the π-bridge between donors and acceptors in these molecules. When a 2,1,3-benzothiadiazole group as a π-bridge was introduced into **CyQN-BTT**, the singlet oxygen yield enhanced to 27.1%, PCE to 37.8%, and the emission wavelength was red-shifted to near-infrared II (NIR-II). Importantly, double-cationic **CyQN-BTT** displays structure-inherent cancer cell targeting ability instead of targeting normal cells. Consequently, relying on NIR-II fluorescence imaging (NIR-II FLI) and photoacoustic imaging (PAI) guided PDT and PTT, **CyQN-BTT** can accurately locate solid tumors in mice and effectively eliminate them with good biocompatibility and biosafety to normal tissues. This study provides insights into the design and development of a tumor-specific targeting multifunctional photosensitizer for precise cancer phototherapy.

## 1 Introduction

Phototheranostics, composed of photodynamic therapy (PDT) and photothermal therapy (PTT) with diagnostic imaging, has received increased attention in recent years due to its non-invasiveness, high precision, and controllability by light.[1–4] In the PDT process, the excited state ($S_1$) energy of photosensitizers (PSs) is activated by light and transferred to the excited triplet state ($T_1$) *via* intersystem crossing (ISC). Then, cytotoxic reactive oxygen species (ROS) are generated *via* energy transfer or electron transfer to ambient oxygen.[5,6] PTT is oxygen-independent and induces light-to-heat conversion to cause tumor cell death *via* non-radiative internal conversion (IC) to the ground state ($S_0$).[7,8] However, the unavoidable oxygen consumption behavior of PDT and the suboptimal photothermal conversion efficiency of PTT make it impossible to effectively kill cancer cells *via* a single phototherapy mode.[3,9,10] Thus, developing combined PDT and PTT in a single-molecule PS (sm-PS) can not only maximize the photon utilization, realizing 1 + 1 > 2 effect[11,12] but also overcome the complex tumor microenvironment and enhance the curative effect to tumor.

In addition, phototheranostic platforms with precise targeting function can improve the bioavailability of PSs, which is crucial for cancer treatment. However, most reported PSs are non-selective and can indiscriminately kill tumor cells and normal cells, which runs counter to precision medicine. The traditional approach is to couple with some functional groups having targeting functions to achieve active targeting of PSs.[13–15] However, after the complex multistep covalent conjugation, the conformation, steric freedom, and orientation of target ligands are always easy to change, which inevitably compromise their binding abilities with the targeting molecule.[16–18] Another strategy is to package PSs into nanoparticles with appropriate size by a nanoprecipitation method, endowing PSs with passive targeting function to tumor regions through enhanced permeability and retention (EPR) effect.[19,20] However, the prepared nanoparticles have low load rate, poor reproducibility, and risk of leakage during transport.[9,21] It is remarkable that the structure-inherent targeting (SIT) strategy can perfectly solve the aforementioned problems. SIT refers to the specific natural targeting ability of the molecule itself, which only relies on the

---

[a] State Key Laboratory of Fine Chemicals, Frontiers Science Center for Smart Materials Oriented Chemical Engineering, Dalian University of Technology, Dalian 116024, China

[b] Ningbo Institute of Dalian University of Technology, Ningbo 315016, China. E-mail: fanjl@dlut.edu.cn

† This work is dedicated to Prof. Xiaojun Peng on the occasion of his 60th birthday.

‡ Electronic supplementary information (ESI) available. See https://doi.org/10.1039/d2sc02879d

inherent structure rather than cross-linking with the targeted ligand or others.[22] In 2018, Fan *et al.* constructed an SIT phototherapy system using the Förster resonance energy transfer mechanism, in which double-cationic features and rhodamine derivatives with a delocalized positive charge were considered to be the key to the production of SIT by photosensitizer molecules.[23] Meanwhile, Zhao *et al.* considered that suitable lipocationic property (*C*log *P*) could endow photosensitizers with specific targeting ability towards cancer cells.[24] In addition, it is well-known that the near-infrared region II FLI (NIR-II FLI, 1000–1500 nm) shows a much higher signal-to-noise ratio, deeper tissue penetration depth, and less light scattering than the well-studied 400–900 nm region FLI, which favors high-quality images to light up tumor areas.[25,26] Meanwhile, photoacoustic imaging (PAI), as another photodiagnosis mode, is a non-invasive and non-ionizing biomedical 3D imaging method that combines the advantages of optical and ultrasound imaging without the influence of photo-scattering, centimeter-level penetration depth, and high spatiotemporal resolution.[27,28] Therefore, the development of sm-PS with SIT features in phototherapy guided by NIR-II FLI and PAI is of great significance, but there is no relevant report so far.

Thus, starting from molecular engineering, we designed and synthesized a series of donor–π–acceptor (D–π–A)-type sm-PSs, **CyE-TT**, **CyQN-TT**, and **CyQN-BTT**, to develop a novel phototheranostic platform with SIT functionality and combined PDT and PTT guided by NIR-II FLI and PAI. At first, 1,1,2-trimethyl-1*H*-benzo[*e*]indole and thiophene-triphenylamine were chosen to construct **CyE-TT** with singlet oxygen generation ability for PDT. The double-cationic group endowed **CyQN-TT** with enhanced water solubility and mitochondrial targeting ability. When 2,1,3-benzothiadiazole (**BTD**) was introduced as a π-bridge, the HOMO–LUMO gap and $\Delta E_{\mathrm{S-T}}$ value of **CyQN-BTT** were simultaneously decreased, which resulted in strong tail emission in NIR-II for NIR FLI and enhanced singlet oxygen generation. In addition, the conjugated skeleton of **CyQN-BTT** became more twisted than **CyE-TT** and **CyQN-TT**, which enhanced the twisted intramolecular charge transfer (TICT) to promote nonradiative transition. More importantly, the double-cationic **CyQN-BTT** has SIT ability to cancer cells instead of normal cells, thus it accurately located solid tumors in mice *via* double-modal imaging and effectively eliminated tumors with combined PDT and PTT.

## 2 Results and discussion

### 2.1 Design and synthesis

In this work, alkyl triphenylamine with a severely twisted skeleton was introduced as a key factor for three purposes: (i) to provide electrons and enhance D–A strength; (ii) to enhance TICT feature to promote nonradiative transition; and (iii) to increase rotor groups to allow the heat energy generation.[29–32] In addition, the D–π–A-type conjugated skeletons displayed an adjustable optical band gap, substantial Stokes shift, low energy levels of ISC, and efficient ROS generation, which have been demonstrated in previous reports.[33,34] What is more, (double-)cationic 1,1,2-trimethyl-1*H*-benzo[*e*]indoles (CyE and CyQN) acted as the electron-deficient acceptor and mitochondrial targeting group, alkyl triphenylamine was the electron-rich and rotor group, and we coupled different conjugated groups (thiophene or/and BTD) as the π-bridge to assemble new D–π–A type sm-PSs (**CyE-TT**, **CyQN-TT**, and **CyQN-BTT**) (Fig. 1A). Chemical structures and synthetic routes are shown in Fig. S1.‡ The target sm-PSs were obtained *via* the Knoevenagel condensation reaction, with brominated alkyl triphenylamine, tin butyl, and boric acid thiophene as the starting materials. Meanwhile, the corresponding intermediates were synthesized through the Suzuki and Stille coupling reaction. An additional quaternary ammonium group was attached to **CyQN-TT** and **CyQN-BTT** to enhance the mitochondrial targeting ability and water solubility. As the π-bridge of electron-deficient **BTD** in **CyQN-BTT** effectively extended the π-conjugated structure and intensified the charge transfer, the emission was red-shifted to NIR-II and the non-radiative transition was facilitated simultaneously. Besides, due to the participation of **BTD**, the $\Delta E_{\mathrm{S-T}}$ value of **CyQN-BTT** was decreased, which was conducive to the ISC process and enhances the photodynamic therapy. Finally, all the structures of intermediate compound and final products were verified *via* NMR, high-resolution mass spectra and FT-IR spectra (Fig. S2–S19 and Table S1‡).

### 2.2 Photophysical properties

**CyE-TT** and **CyQN-TT** had similar absorption spectra, and the maximal absorption wavelength was 620 nm (Fig. 1B). When **BTD** was incorporated into the conjugated skeleton, the absorption wavelength of **CyQN-BTT** was red-shifted to 677 nm due to the conjugated structure extension and electron-deficient properties of **BTD**.[35] It is worth mentioning that **CyQN-BTT** has a broad absorption peak (420–840 nm), considering the comparison with **CyE-TT** and **CyQN-TT** at the same excitation wavelength; we chose 671 nm laser as the excitation light source of the sm-PSs. In addition, the maximum emission wavelength excited by 671 nm was red-shifted from 764 nm (**CyQN-TT**) to 938 nm (**CyQN-BTT**) (Fig. 1C). Notably, the tail emission of **CyQN-BTT** extended to the NIR-II region, which was beneficial to high-quality NIR-II FLI. Based on this, we evaluated the NIR-II fluorescence emission intensity of **CyQN-BTT** in a concentration- and long-pass-filter-dependent manner (Fig. S19‡). As the concentration increased, the fluorescence signal was gradually enhanced. A significant fluorescence signal was observed even at the 1150 nm filter. These evidences suggested that photosensitizers might have aggregation-induced emission (AIE) properties, which might be related to the motion limitation of triphenylamine.[1,6,27,31,33] Finally, we investigated and evaluated the FL features of **CyE-TT**, **CyQN-TT**, and **CyQN-BTT** using toluene (PhMe)/DMSO mixtures with different PhMe fractions ($f_{\mathrm{w}}$) as solvents (Fig. 1D and S20‡). The fluorescence signal of **CyE-TT**, **CyQN-TT**, and **CyQN-BTT** could be detected in DMSO with an absolute fluorescence quantum yield of only 0.5%, 0.3%, and 0.12% (Table S2‡). Upon $f_{\mathrm{w}}$ increasing to 99% (even $f_{\mathrm{w}}$ = 100%), the fluorescence intensities increased significantly with an absolute fluorescence quantum yield of 14.5%, 13.9%, and 4.6% for **CyE-TT**, **CyQN-TT**, and **CyQN-BTT**, respectively,

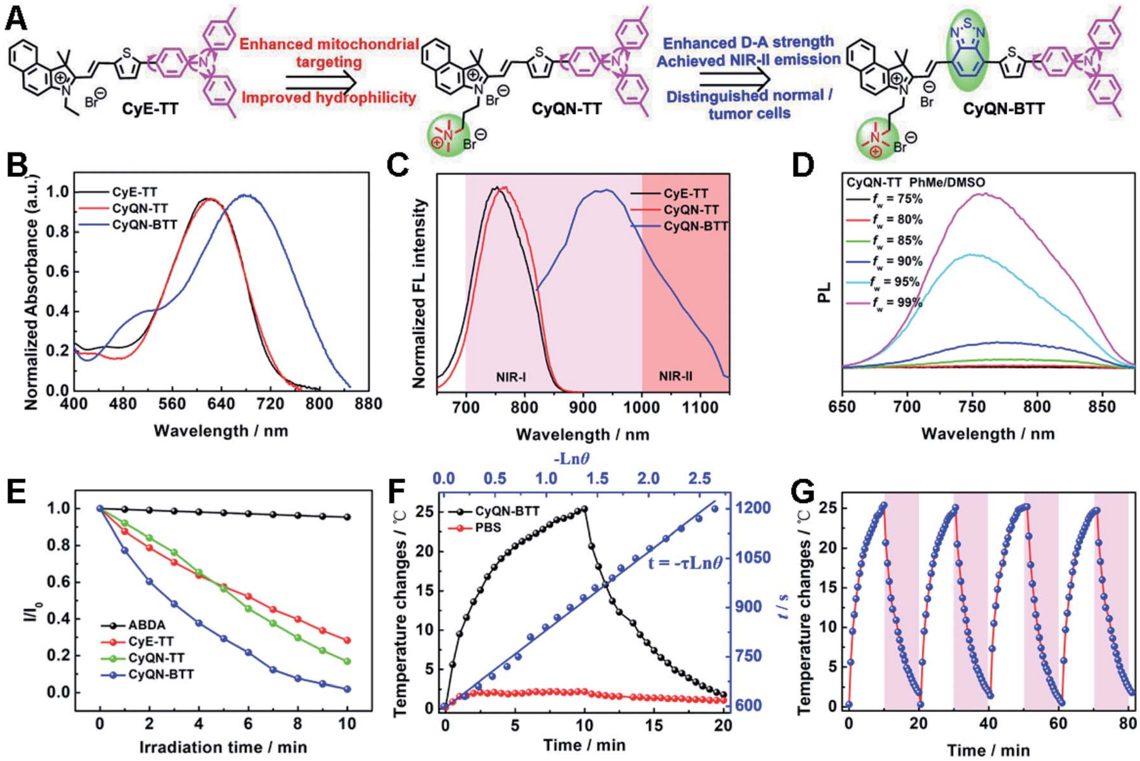

Fig. 1 (A) Molecular structures, (B) normalized absorption (in DMSO), and (C) normalized FL intensity (in PhMe) of **CyE-TT**, **CyQN-TT**, and **CyQN-BTT**. (D) FL feature of **CyQN-TT** in PhMe/DMSO mixtures with different toluene fractions ($f_W$). (E) $^1O_2$ generation of **CyE-TT**, **CyQN-TT**, and **CyQN-BTT** with ABDA as indicators under 671 nm laser irradiation. (F) Photothermal curves of **CyQN-BTT** with/without laser irradiation (671 nm, 0.4 W cm$^{-2}$) and the linear fitting of time and negative logarithmic function of driving force temperature change. (G) Photothermal stability curves of **CyQN-BTT** under four irradiation–cooling cycles.

which was beneficial for FLI-guided phototherapy. The fluorescence intensity and absolute fluorescence quantum yield of **CyQN-BTT** were significantly lower than the other two because its more twisted intramolecular charge transfer (TICT) shortened the radiative transition.[1,31,32,35]

### 2.3 $^1O_2$ generation and the evaluation of photothermal conversion efficiency

Commercial 9,10-anthracenediyl-bis(methylene)-dimalonic acid (ABDA) as a $^1O_2$ indicator can be oxidized by $^1O_2$ accompanied by a gradually decreasing absorption spectra. As shown in Fig. 1E and S21,‡ under laser irradiation in the sm-PS solution, the absorption spectra of ABDA gradually decreased, which meant $^1O_2$ generation. After 10 min of laser irradiation, the absorbance of ABDA nearly vanished. In contrast, the absorption spectra of ABDA without sm-PSs had no loss after 10 min of laser irradiation. The results indicate that three sm-PSs could consume energy *via* the ISC pathway to generate $^1O_2$ for PDT. With methylene blue as the reference, the singlet oxygen yields of **CyE-TT**, **CyQN-TT**, and **CyQN-BTT** were 21.3%, 22.0% and 27.1%, respectively. For the photothermal performances of **CyE-TT**, **CyQN-TT**, and **CyQN-BTT** under laser irradiation, their temperatures rose 11.6 °C, 13.0 °C, and 22.7 °C, respectively, which indicated that the addition of **BTD** was beneficial to the improvement of photothermal conversion performance (Fig. S22‡). A concentration-dependent temperature increment occurred when different concentrations of **CyQN-BTT** were irradiated by a fixed laser power density (0.4 W cm$^{-2}$). Similarly, the temperature changes were also positively correlated with laser power (Fig. S23‡), favoring reasonable temperature regulation. Among the three sm-PSs, **CyQN-BTT** exhibited the best PTT performance with a photothermal conversion efficiency (PCE) of 37.8% (Fig. 1F and S24‡), which is higher than most reported photothermal agents.[1,36,37] After four irradiation–cooling cycles, there was little change in the temperature platform of **CyQN-BTT** (Fig. 1G), indicating excellent photothermal stability, which was also proved with melting point data (Fig. S25‡).

### 2.4 Theory model analysis

The density functional theory (DFT) was used to explain the distinctions in photophysics and photochemistry among **CyE-TT**, **CyQN-TT**, and **CyQN-BTT**. The negligible difference in HOMO–LUMO between **CyE-TT** and **CyQN-TT** is demonstrated in Fig. 2A and Table S3.‡ However, the extended π-conjugated skeleton and enhanced electron-deficient properties supplied **CyQN-BTT** with lower LUMO (−3.42 eV) and narrower HOMO–LUMO energy levels (2.81 eV). Furthermore, there were smaller $\Delta E_{S-T}$ values (0.48 eV) in **CyQN-BTT** than in **CyE-TT** and **CyQN-TT**, consistent with the previously reported theory that tuning the HOMO–

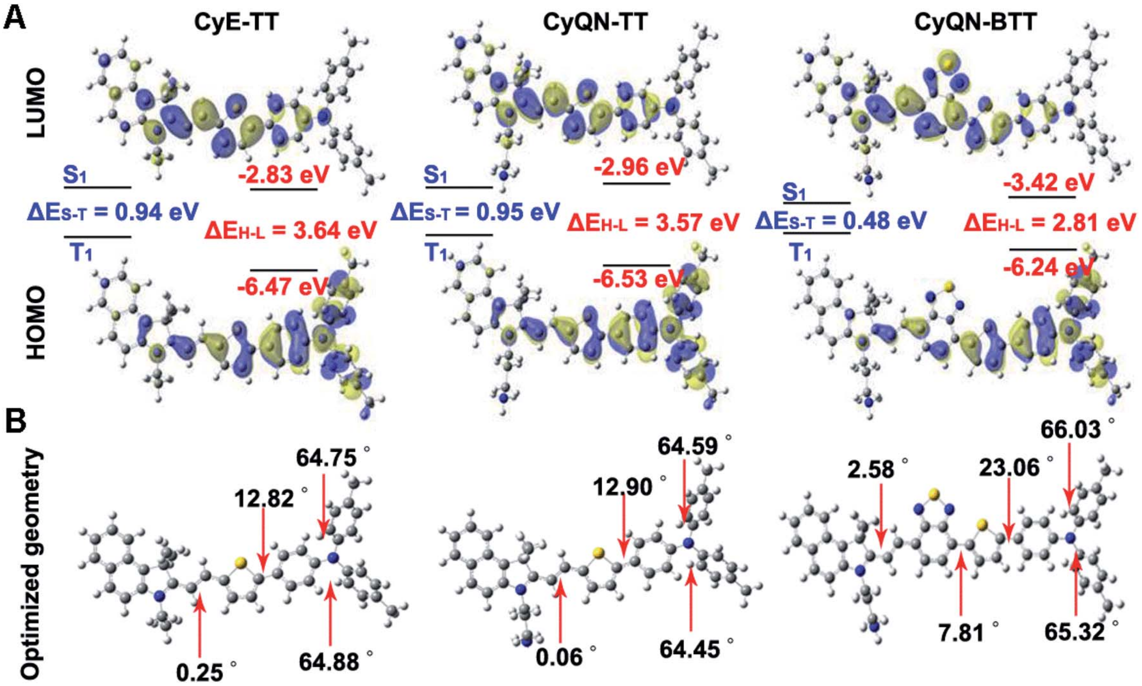

Fig. 2 Theory model analysis of **CyE-TT**, **CyQN-TT**, and **CyQN-BTT** by density functional theory. (A) HOMO–LUMO distribution and $\Delta E_{S-T}$ values. (B) Optimization geometries and the dihedral angle distribution.

LUMO separation can regulate non-radiative transition.[31,32,38] However, the addition of **BTD** increased the steric hindrance effect, resulting in a more twisted, conjugated skeleton of **CyQN-BTT** with a dihedral angle of 7.81° (between the plane of **BTD** and thiophene), 23.06° (between the plane of thiophene and adjacent benzene ring), and 65.32–66.03° that existed in triphenylamine (Fig. 2B). This result also explains why the PCE of **CyQN-BTT** was the highest among the three sm-PSs. Thus, the high-performance phototherapy properties of **CyQN-BTT** could be attributed to several factors: (i) the strong D–A relationship reduced HOMO–LUMO energy levels and promoted the ISC efficiency;[33–35,39] (ii) the twisted conformation provided some space for the active rotor motion to enhance the PCE;[31,35,36] and (iii) the twisted conformation enhanced TICT feature.[31,32,35]

### 2.5 Targeting ability and phototherapy *in vitro*

As shown in Fig. 3A, B and S26–S30,‡ **CyE-TT** and **CyQN-TT** were quickly taken up by tumor cells (MCF-7 cells) and normal cells (3T3 cells), respectively, within 2 h. Furthermore, the fluorescence signals of **CyE-TT** and **CyQN-TT** were overlapped with that of the Mito-green tracker, indicating an excellent mitochondrial-targeting function (the Pearson's correlation coefficients [*r*] exceeding 0.85). However, a bright **CyQN-BTT** fluorescence signal was detected on the cell membrane and mitochondria of MCF-7 cells and barely detected on the 3T3

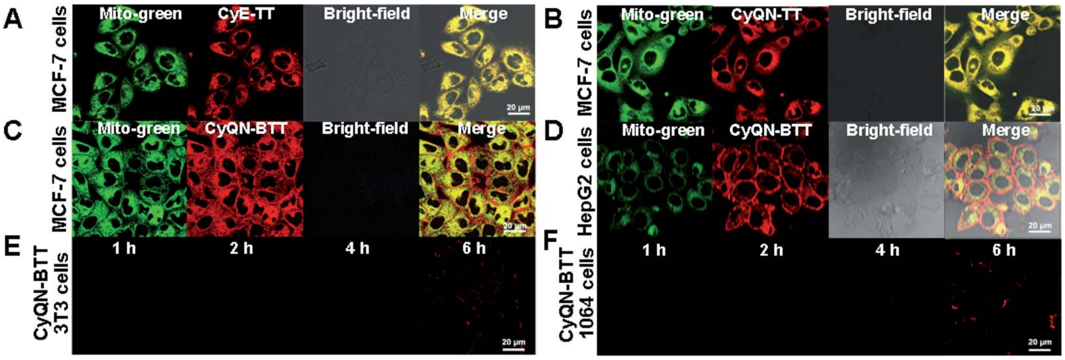

Fig. 3 Colocation analysis with a Mito-green tracker and (A) **CyE-TT**, (B) **CyQN-TT**, and (C) **CyQN-BTT** in MCF-7 cells. Intracellular fluorescence intensity of **CyQN-BTT** at different times in 3T3 cells (D) and 1064 cells (F). Colocation analysis with a Mito-green tracker and (E) **CyQN-BTT** in HepG2 cells. sm-PSs concentration = 10.0 μL, 1.0 mg mL$^{-1}$; cell concentration = ~10$^{6}$ mL$^{-1}$; the error bar represents the standard deviation (SD) of the three groups of parallel experimental data (mean ± SD, $n = 3$); scale bar = 20 μm.

cells, even after 6 h (Fig. 3C, D and S31‡). Moreover, in other cancer cells (HepG2 cells) and normal cells (1064 cells), the same phenomenon was observed (Fig. 3E, F, S32 and S33‡). These results indicated that **CyQN-BTT** had SIT features towards tumor cells instead of normal cells. For these phenomena, we suspected that it might be caused by the following factors: (i) more electronegative character of cancer cells than normal cells has been proved, and the double-cationic group of **CyQN-BTT** is more likely to gravitate toward more electronegative cancer cells;[23,40–42] (ii) the primary driving force for normal cells is hydrophobicity, while that for cancer cells is the electrostatic interaction;[42] (iii) there is a stronger electrostatic interaction between the more electronegative cancer cells and the double-cationic group of **CyQN-BTT**; (iv) the *C*log *P* (oil–water partition coefficients) value of **CyQN-BTT** (10.60) is less than that of **CyE-TT** (14.62) and **CyQN-TT** (14.61), which may facilitate access to cancer cells and limit access to normal cells.[43]

DCFH-DA itself has no fluorescence in cells but emits bright green fluorescence when triggered by ROS to produce DCF. Thus, DCFH-DA, as an intracellular $^1O_2$ tracker, was co-incubated with MCF-7 cells and sm-PSs. As shown in Fig. 4A and S34,‡ after 20 min of co-incubation, a bright green fluorescence was observed under laser irradiation for 2 min, representing the $^1O_2$ production. In addition, we used Calcein-AM (stains live cells with green fluorescence signal) and PI (stains dead cells with red fluorescence signal) to stain normal (3T3 cells) and cancer (4T1 cells) cells, respectively, to evaluate the phototoxicity and dark toxicity of the three sm-PSs (Fig. 4B, D, S35 and S36‡). All sm-PSs could easily enter the cancer cells, and the 4T1 cells were killed, which exhibited red fluorescence after laser irradiation. In comparison, all the control groups showed green fluorescence, indicating the negligible cytotoxicity of sm-PSs or laser irradiation. Because **CyE-TT** and **CyQN-TT** could enter cancer cells and normal cells indiscriminately, the 3T3 cells exhibited similar phototherapy effects. However, we observed bright green fluorescence and negligible red fluorescence in **CyQN-BTT**, and the laser radiation (Fig. 4C) explained the SIT function of **CyQN-BTT**. Finally, we examined the viability of the 4T1 and 3T3 cells with sm-PS concentration dependence *via* an MTT assay (Fig. 4E–G). In the darkness, the viability of the 4T1 and 3T3 cells remained unchanged (more than 95%). In comparison, it was significantly decreased (as low as 10%) under laser irradiation and increasing concentrations of **CyE-TT** and **CyQN-TT**, consistent with the results of the live/dead cell staining experiments. The half-maximal inhibitory concentration ($IC_{50}$) values of **CyE-TT** and **CyQN-TT** were calculated as 9.45 and 8.78 μg mL$^{-1}$ for the 4T1 cells; 8.01 and 8.52 μg mL$^{-1}$ for the 3T3 cells, respectively (Fig. S37‡). Due to the excellent phototherapy ability and SIT ability, we explored the MTTs of **CyQN-BTT** for 4T1 and 3T3 cells. Under a laser power density of 0.1 W cm$^{-2}$, **CyQN-BTT** had only a PDT function, and >90% of the 4T1 cells were killed. Vitamin C (VC) can effectively scavenge $^1O_2$.[23] When VC was added under 0.4 W cm$^{-2}$ of laser power density, **CyQN-BTT** had only a PTT function and showed foreseeable phototoxicity for the 4T1 cells. However, **CyQN-BTT**, under a laser power density of 0.4 W cm$^{-2}$, displayed PDT and PTT properties and much higher phototoxicities by killing up to 95% of the 4T1 cells and an $IC_{50}$ value of 9.45 μg mL$^{-1}$. On the contrary, we observed negligible phototoxicity of **CyQN-BTT** for the 3T3 cells (Fig. 4G), whether it was under only PDT, PTT, or combined phototherapy conditions. Due to the excellent PDT and PTT, as well as SIT ability for tumor cells, the *in vivo*

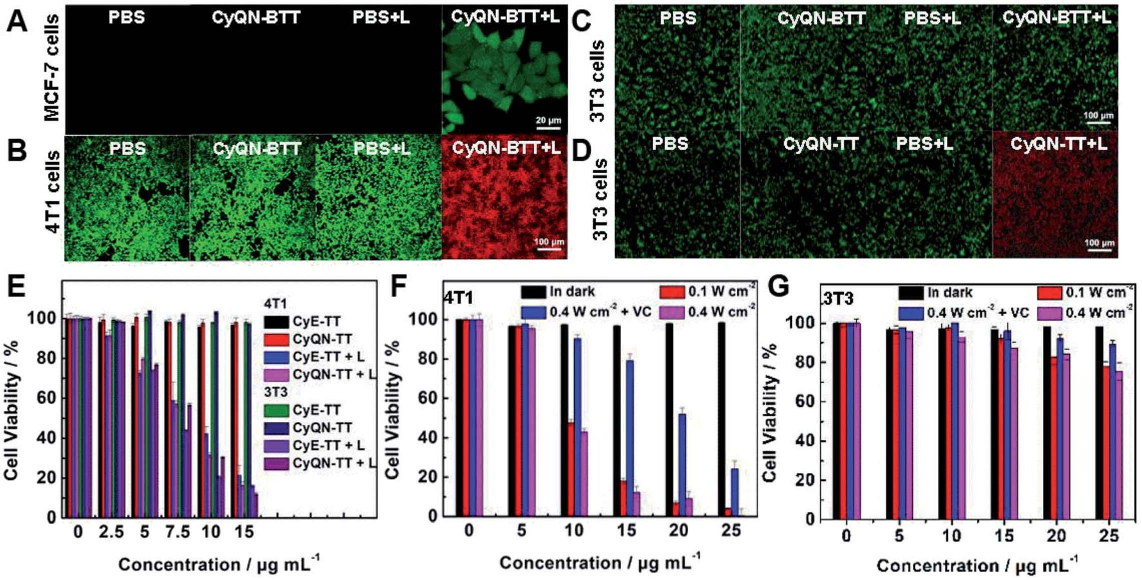

Fig. 4 (A) Intracellular ROS generation with DCFH-DA as an indicator in MCF-7 cells coincubated with **CyQN-BTT**. Scale bar = 20 μm. Live/dead cell staining of (B) 4T1 cells and (C) 3T3 cells coincubated with **CyQN-BTT**, and (D) 3T3 cells coincubated with **CyE-TT** under 671 nm laser irradiation (0.4 W cm$^{-2}$). sm-PS concentration = 10.0 μL, 1.0 mg mL$^{-1}$; cell concentration = ~10$^6$ mL$^{-1}$; mean ± SD ($n$ = 3); scale bar = 100 μm. (E–G) Assessment of phototoxicity and dark toxicity of **CyE-TT**, **CyQN-TT**, and **CyQN-BTT** for 4T1 and 3T3 cells by an MTT assay. Mean ± SD ($n$ = 5).

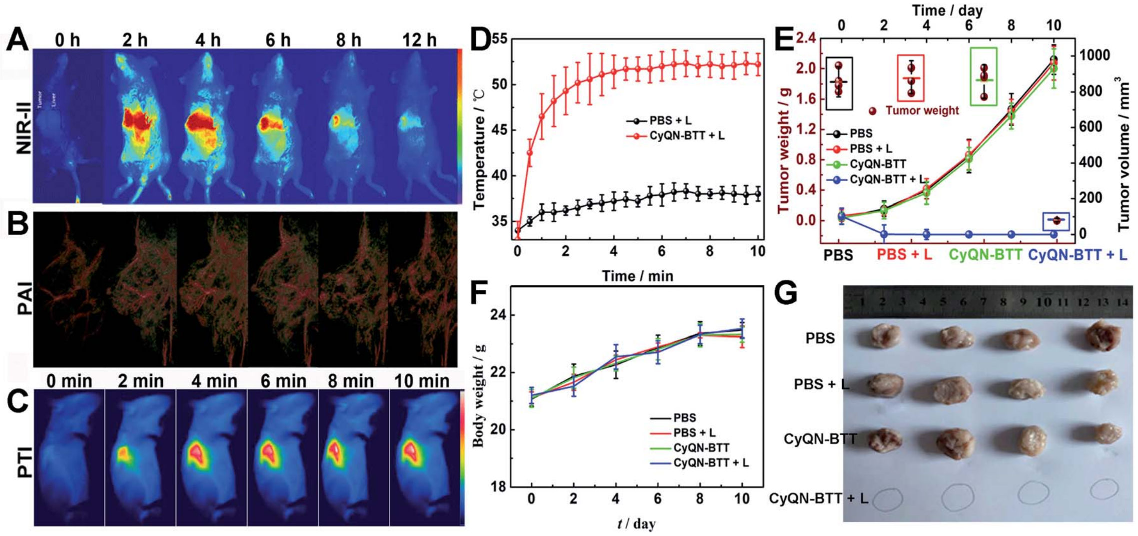

Fig. 5 (A) NIR-II FLI, and (B) PAI for 4T1-bearing mice at different times after injection of **CyQN-BTT** (100 μL, 1 mg mL$^{-1}$). (C) PTI of 4T1-bearing mice at different times after **CyQN-BTT** injection (4 h later) by laser irradiation. (D) Temperature changes of mice under laser illumination. The change in (E) tumor volume and weight, and (F) body weight of mice during treatment. (G) Photographs of 4T1 tumor after 10 days of treatment. Mean ± SD, $n = 4$.

experiments were carried out with **CyQN-BTT** as the phototherapy reagent.

## 2.6 Phototheranostics *in vivo*

Given the tail emission in the NIR-II regions and satisfactory PCE of **CyQN-BTT**, we investigated NIR-II FLI and PAI-guided combined phototherapy. NIR-II FLI (long-pass filter of 1050 nm) *in vivo* showed a fairly low background fluorescence (Fig. 5A), which was beneficial for accurately distinguishing tumors from normal tissues.[25,26] The NIR-II fluorescence signal reached a maximum at 4 h, and the bright fluorescence was still observed at 12 h. It is worth noting that the fluorescence signal within the liver was clearly captured, which means that the liver may metabolize nanoparticles. Based on this, 4 h was considered the optimal phototherapy time. Moreover, the photoacoustic signal of hemoglobin within the blood vessels at the tumor region was clearly observed (Fig. 5B). Until 4 h, the signal reached a maximum plateau and remained up to 12 h, which was consistent with the results of NIR-II FLI. Eight hours after

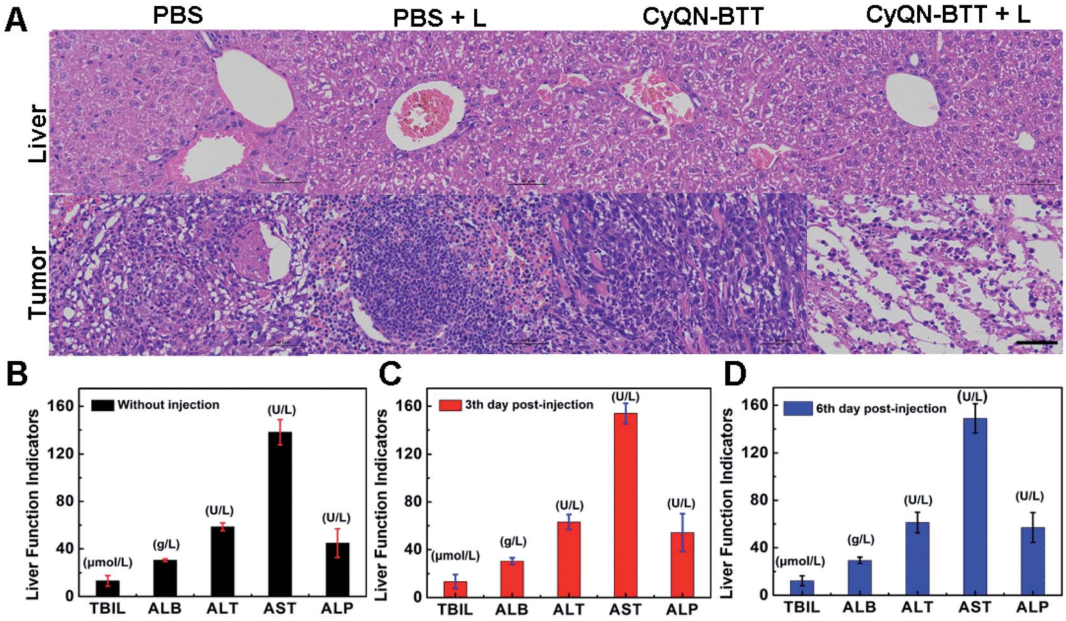

Fig. 6 (A) Hematoxylin and eosin (H&E) of liver and tumors treated under different conditions. Scale bar = 50 μm. (B–D) Hematological assessment of liver function indicators of mice at different post-injection times. Mean ± SD, $n = 4$.

the injection, we dissected the principal organs of the mice to explore the distribution of **CyQN-BTT** *in vivo*. The results (Fig. S38‡) indicate that **CyQN-BTT** was mainly distributed in the tumor and liver, because the liver is the main metabolic organ.

Based on the above-mentioned results, tumor-bearing mice were irradiated at 6 h after the tail vein injection of **CyQN-BTT** (only a single-dose injection for phototherapy). As illustrated in Fig. 5C, D and S39,‡ upon laser irradiation, the temperature in the phototherapy group increased rapidly to 52 °C with negligible changes in the control groups. After the laser irradiation, we continuously monitored the changes in body weight and tumor volume of all mice for 10 days to estimate the phototherapy outcome. On the third day after laser irradiation, the tumor in the phototherapy group was almost eliminated, and there was no recurrence within 10 days, as shown in Fig. 5E–G. In contrast, the tumor volume and weight of the mice in the control groups increased up to 12-fold and 2.8-fold by day 10, respectively. Furthermore, the weight of all mice in the four groups was consistent, which revealed the excellent biosafety of **CyQN-BTT**. H&E staining of the major organs and tumors dissected from mice was performed and analyzed (Fig. 6A and S40‡). We found no apparent damage in the major organs (heart, liver, spleen, kidney, and lung) of the mice in the four groups but severely necrotic tumor tissue in the phototherapy group. Simultaneously, there were no abnormal liver function indexes before and after treatment (Fig. 6B–D), which showed that **CyQN-BTT** has no negative consequence on the functions of the liver.

## 3 Conclusion

We combined two different quaternized 1,1,2-trimethyl-1*H*-benz[*e*]indoles as acceptors, twisted alkyl triphenylamine as a donor and rotor, and (**BTD**) thiophene as a π bridge to synthesize a series of D–π–A-type sm-PSs (**CyE-TT**, **CyQN-TT**, and **CyQN-BTT**). These sm-PSs displayed bright NIR-I emission, good mitochondrial targeting, and satisfactory PDT function. Because the addition of **BTD** enhanced the push–pull effect, the emission spectra of **CyQN-BTT** red-shifted further into the NIR-II region. The smaller $\Delta E_{\text{S-T}}$ value and twisted conjugated skeleton supplied the **CyQN-BTT** with a more efficient $^1O_2$ generation for PDT and a higher PCE of 37.8% for PTT than that of **CyE-TT** and **CyQN-TT**. Moreover, due to the double-cationic feature, **CyQN-BTT** showed excellent SIT ability for cancer cells instead of normal cells. Finally, using **CyQN-BTT** as a sm-PS, the tumor tissue was precisely located and visibly delineated through NIR-II FLI and PAI, and effectively eliminated by combined PDT and PTT. In addition, **CyQN-BTT** showed good biocompatibility for normal tissues and organs. These findings can provide new ideas for developing a specifically targeted phototherapy platform.

## Data availability

The ESI‡ include the synthesis, NMR and high-resolution mass spectrometry of photosensitizers, the experiment of cell uptake, AIE feature, PDT, PTT, live/dead cell staining, mouse phototherapy, biosafety tests, *etc.*

## Author contributions

H. Gu designed and performed all the experiments and wrote the manuscript. W. J. Liu carried out and participated in TOC drawing and experimental data analysis. J. L. Fan directed the whole process in this work, guided the writing and revised the manuscript. J. L. Fan, W. Sun, J. J. Du, and X. J. Peng offered constructive suggestions on improvement of this work and provided the financial support.

## Conflicts of interest

The authors declare that they have no conflict of interest.

## Acknowledgements

This work was financially supported by the National Natural Science Foundation of China (21925802, 21878039, 21808028, 22022803, 22078046), the NSFC-Liaoning United Fund (U1908202), National Key Research and Development Plan (2018AAA0100301), and the Fundamental Research Funds for the Central Universities (DUT22LAB601). This study was conducted in accordance with the Guide for the Care and Use of Laboratory Animals published by the US National Institutes of Health (8th edition, 2011). The animal protocol was approved by the local research ethics review board of the Animal Ethics Committee of Dalian University of Technology.

## References

1 G. X. Feng, G. Q. Zhang and D. Ding, *Chem. Soc. Rev.*, 2020, **49**, 8179–8234.
2 Y. Cai, W. L. Si, W. Huang, P. Chen, J. J. Shao and X. C. Don, *Small*, 2018, **14**, 1704247.
3 X. Y. Deng, Z. W. Shao and Y. L. Zhao, *Adv. Sci.*, 2021, **8**, 2002504.
4 Z. Yang and X. Y. Chen, *Acc. Chem. Res.*, 2019, **52**, 1245–1254.
5 D. Dolmans, D. Fukumura and R. K. Jain, *Nat. Rev. Cancer*, 2003, **3**, 380–387.
6 C. Chen, H. L. Ou, R. H. Liu and D. Ding, *Adv. Mater.*, 2020, **32**, 1806331.
7 H. D. Li, H. Kim, F. Xu, J. J. Han, Q. C. Yao, J. Y. Wang, K. Y. Pu, X. J. Peng and J. Yoon, *Chem. Soc. Rev.*, 2022, **51**, 1795–1835.
8 J. Q. Chen, C. Y. Ning, Z. N. Zhou, P. Yu, Y. Zhu, G. X. Tan and C. B. Mao, *Prog. Mater. Sci.*, 2019, **99**, 1–26.
9 B. Nasseri, E. Alizadeh, F. Bani, S. Davaran, A. Akbarzadeh, N. Rabiee, A. Bahadori, M. Ziaei, M. Bagherzadeh, M. R. Saeb, M. Mozafari and M. R. Hamblin, *Appl. Phys. Rev.*, 2022, **9**, 011317.
10 S. S. Ding, L. He, X. W. Biana and G. Tian, *Nano Today*, 2020, **35**, 100920.

11 W. Zhu, M. M. Kang, Q. Wu, Z. J. Zhang, Y. Wu, C. B. Li, K. Li, L. Wang, D. Wang and B. Z. Tang, *Adv. Funct. Mater.*, 2020, 2007026.

12 Y. F. Wang, Y. D. Sun, J. B. Ran, H. R. Yang, S. Z. Xiao, J. Yang, C. Y. Yang, H. M. Wang and Y. Liu, *ACS Appl. Mater. Interfaces*, 2022, **14**, 225–235.

13 M. L. Li, J. Xia, R. S. Tian, J. Y. Wang, J. L. Fan, J. J. Du, S. R. Long, X. Z. Song, J. W. Foley and X. J. Peng, *J. Am. Chem. Soc.*, 2018, **140**, 14851–14859.

14 U. Goswami, A. Dutta, A. Raza, R. Kandimalla, S. Kalita, S. S. Ghosh and A. Chattopadhyay, *ACS Appl. Mater. Interfaces*, 2018, **10**, 3282–3294.

15 H. S. Choi, S. L. Gibbs, J. H. Lee, S. H. Kim, Y. Ashitate, F. B. Liu, H. Hyun, G. L. Park, Y. Xie, S. Bae, M. Henary and J. V. Frangioni, *Nat. Biotechnol.*, 2013, **31**, 148–153.

16 C. M. Paulos, J. A. Reddy, C. P. Leamon, M. J. Turk and P. S Low, *Mol. Pharmacol.*, 2004, **66**, 1406–1414.

17 Z. L. Cheng, A. Al Zaki, J. Z. Hui, V. R. Muzykantov and A. Tsourkas, *Science*, 2012, **338**, 903.

18 J. A. Mackintosh, H. M. Marshall and K. M. Fong, *J. Thorac. Oncol.*, 2019, **14**, 577–579.

19 S. Wilhelm, A. J. Tavares, Q. Dai, S. Ohta, J. Audet, H. F. Dvorak and W. C. W. Chan, *Nat. Rev. Mater.*, 2016, **1**, 16014.

20 J. Park, Y. Choi, H. Chang, W. Um, J. H. Ryu and I. C. Kwon, *Theranostics*, 2019, **9**, 8073–8090.

21 E. Blanco, H. F. Shen and M. Ferrari, *Nat. Biotechnol.*, 2015, **33**, 941–951.

22 H. Hyun, M. H. Park, E. A. Owens, H. Wada, M. Henary, H. J. M. Handgraaf, A. L. Vahrmeijer, J. V. Frangioni and H. S. Choi, *Nat. Med.*, 2015, **21**, 192–197.

23 M. L. Li, S. R. Long, Y. Kang, L. Y. Guo, J. Y. Wang, J. L. Fan, J. J. Du and X. J. Peng, *J. Am. Chem. Soc.*, 2018, **140**, 15820–15826.

24 Y. Li, J. B. Zhuang, Y. Lu, N. Li, M. J. Gu, J. Xia, N. Zhao and B. Z. Tang, *ACS Nano*, 2021, **15**, 20453–20465.

25 S. J. Zhu, R. Tian, A. L. Antaris, X. Y. Chen and H. J. Dai, *Adv. Mater.*, 2019, **31**, 1900321.

26 A. M. Smith, M. C. Mancini and S. M. Nie, *Nat. Nanotechnol.*, 2009, **4**, 710–711.

27 J. Qi, N. Alifu, A. Zebibula, P. Wei, J. W. Y. Lam, H.-Q. Peng, R. T. K. Kwok, J. Qian and B. Z. Tang, *Nano Today*, 2020, **34**, 100893.

28 Y. C. Liu, L. L. Teng, B. L. Yin, H. M. Meng, X. Yin, S. Y. Huan, G. S. Song and X.-B. Zhang, *Chem. Rev.*, 2022, **122**, 6850–6918.

29 H. Chen, Y. P. Wan, X. Cui, S. L. Li and C.-S. Le, *Adv. Healthcare Mater.*, 2021, **10**, 2101607.

30 Z. Y. Jiang, C. L. Zhang, X. Q. Wang, M. Yan, Z. X. Ling, Y. C. Chen and Z. P. Liu, *Angew. Chem., Int. Ed.*, 2021, **60**, 22376–22384.

31 L. Q. Liu, X. Wang, L.-J. Wang, L. Q. Guo, Y. B. Li, B. Bai, F. Fu, H. G. Lu and X. W. Zhao, *ACS Appl. Mater. Interfaces*, 2021, **13**, 19668–19678.

32 Z. J. Zhang, W. H. Xu, M. M. Kang, H. F. Wen, H. Guo, P. F. Zhang, L. Xi, K. Li, L. Wang, D. Wang and B. Z. Tang, *Adv. Mater.*, 2020, **32**, 2003210.

33 Z. Zheng, T. Zhang, H. Liu, Y. Chen, R. T. K. Kwok, C. Ma, P. Zhang, H. H. Y. Sung, I. D. Williams, J. W. Y. Lam, K. S. Wong and B. Z. Tang, *ACS Nano*, 2018, **12**, 8145–8159.

34 Q. Wan, R. Y. Zhang, Z. Y. Zhuang, Y. X. Li, Y. H. Huang, Z. M. Wang, W. J. Zhang, J. Q. Hou and B. Z. Tang, *Adv. Funct. Mater.*, 2020, 2002057.

35 C. Wang, Q. L. Qiao, W. J. Chi, J. Chen, W. J. Liu, D. Tan, S. McKechnie, D. Lyu, X.-F. Jiang, W. Zhou, N. Xu, Q. S. Zhang, Z. C. Xu and X. G. Liu, *Angew. Chem., Int. Ed.*, 2020, **59**, 10160–10172.

36 H. S. Jung, P. Verwilst, A. Sharma, J. Shin, J. L. Sessler and J. S. Kim, *Chem. Soc. Rev.*, 2018, **47**, 2280–2297.

37 H. Lin, Y. W. Wang, S. S. Gao, Y. Chen and J. L. Shi, *Adv. Mater.*, 2018, **30**, 1703284.

38 M. M. Kang, C. C. Zhou, S. M. Wu, B. R. Yu, Z. J. Zhang, N. Song, M. M. S. Lee, W. H. Xu, F.-J. Xu, D. Wang, L. Wang and B. Z. Tang, *J. Am. Chem. Soc.*, 2019, **141**, 16781–16789.

39 T. F. Zhang, J. Y. Zhang, F.-B. Wang, H. Cao, D. M. Zhu, X. Y. Chen, C. H. Xu, X. Q. Yang, W. B. Huang, Z. Y. Wang, J. F. Wang, Z. K. He, Z. Zheng, J. W. Y. Lam and B. Z. Tang, *Adv. Funct. Mater.*, 2022, 2110526.

40 M. L. Li, T. Xiong, J. J. Du, R. S. Tian, M. Xiao, L. Y. Guo, S. R. Long, J. L. Fan, W. Sun, K. Shao, X. Z. Song, J. W. Foley and X. J. Peng, *J. Am. Chem. Soc.*, 2019, **141**(6), 2695–2702.

41 M. Y. Wu, M. J. Gu, J. K. Leung, X. M. Li, Y. C. Yuan, C. Shen, L. R. Wang, E. G. Zhao and S. J. Chen, *Small*, 2021, 2101770.

42 G. R. Li, Y. B. Huang, Q. Feng and Y. X. Chen, *Molecules*, 2014, **19**, 12224–12241.

43 R. W. Horobin, J. C. Stocker and F. Rashid-Doubell, *Histochem. Cell Biol.*, 2013, **139**, 623–637.